Water Research 203 (2021) 117545

Contents lists available at ScienceDirect

Water Research

journal homepage: www.elsevier.com/locate/watres

Solar irradiation induced oxidation and adsorption of arsenite on natural pyrite

Lihu Liu [a], Diman Guo [a], Zengping Ning [b], Chengshuai Liu [b], Guohong Qiu [a,*]

[a] Key Laboratory of Arable Land Conservation (Middle and Lower Reaches of Yangtse River), Ministry of Agriculture and Rural Affairs, Hubei Key Laboratory of Soil Environment and Pollution Remediation, State Environmental Protection Key Laboratory of Soil Health and Green Remediation, College of Resources and Environment, Interdisciplinary Sciences Institute, Huazhong Agricultural University, Wuhan 430070, Hubei Province, China

[b] State Key Laboratory of Environmental Geochemistry, Institute of Geochemistry, Chinese Academy of Sciences, Guiyang 550081, Guizhou Province, China

ARTICLE INFO

Keywords:
Pyrite
Arsenite
Arsenate
Solar irradiation
Reactive oxygen species

ABSTRACT

The migration and bioavailability of toxic elemental arsenic (As) are influenced by the adsorption and redox processes of sulfide minerals in waters around mining areas. Pyrite is the most abundant sulfide mineral in the Earth's crust and exhibits certain photochemical activity. However, the adsorption and redox behaviors of arsenite (As(III)) on pyrite surface under solar irradiation remain unclear. Here, the interaction between As(III) and natural pyrite was investigated under light irradiation. The results indicated that solar irradiation promotes As(III) oxidation and adsorption on pyrite surface due to reactive oxygen species (ROS) intermediates. The reactions between H_2O/O_2 and hole–electron pairs (h_{vb}^+–e_{cb}^-) on excited pyrite and the oxidation of Fe^{2+} released from pyrite by dissolved O_2 contributed much to the generation of $OH^•$, $O_2^{•-}$ and H_2O_2 under light irradiation. ROS production and As(III) oxidation were accelerated by dissolved O_2. An increase in pH within 5.0 to 9.0 decreased the concentration of $OH^•$ but increased that of H_2O_2 and the amount of oxidized As(III). In weakly acidic and neutral environments, $OH^•$ was mainly responsible for As(III) oxidation, while H_2O_2 contributed much to As(III) oxidation in weakly alkaline environments. Partial arsenate (As(V)) was adsorbed on pyrite and newly formed ferrihydrite. The present work enriches the understanding of As migration and transformation in the waters around mining areas, and provides a potential method for As(III) removal by using pyrite under solar irradiation.

1. Introduction

Arsenic (As), a metalloid element with high toxicity and strong carcinogenicity, is conmonly found in environments (Wei et al., 2019a; Wei et al., 2019b). In addition to geological activities, mining, underground construction and other human activities are important causes of As pollution (Ho et al., 2021; Tabelin et al., 2014; Tabelin et al., 2010; Tamoto et al., 2015). Although the crustal abundance of As is only 0.0001% (Oremland and Stolz, 2003), high levels of As can be detected in some sulfide minerals, soluble salts, organic matter and sedimentary rocks (Huyen et al., 2019; Tabelin et al., 2018; Tabelin et al., 2017). For instance, the content of As can reach up to 45wt.% in arsenopyrite (Paikaray, 2014). In abandoned ore deposits, waste rock dumps and tailing overburdens, the oxidation of As-containing sulfide minerals is generally accompanied by the desorption and release of As, resulting in As pollution in mining wastewater, which can indirectly affect the surrounding rivers and groundwaters (Park et al., 2019; Rodriguez-Lado et al., 2013; Zhang et al., 2017).

The toxity and mobility of As vary with its existing form in waters. The main species of inorganic As in oxic water environments are arsenates ($H_2AsO_4^-$ and $HAsO_4^{2-}$), while arsenites ($H_2AsO_3^-$ and H_3AsO_3) are more ubiquitous in anoxic water environments (Cuong et al., 2021; Oremland and Stolz, 2003). Generally, As(III) is dozens of times more toxic to humans than As(V), and arsenite has a lower adsorption capacity on various adsorbents than arsenate, resulting in its higher mobility in water environments (Bhandari et al., 2011; Canas Kurz et al., 2021). Therefore, the migration and transformation of As(III) in the mine and the surrounding water environment have been hot spots of research in environmental chemistry (Hiller et al., 2012; Hong et al., 2020; Le Pape et al., 2017).

Pyrite is the most abundant sulfide mineral in the Earth's crust (Diao et al., 2013; Zhang and Yuan, 2017). The trap of As by pyrite in

* Corresponding author.
E-mail address: qiugh@mail.hzau.edu.cn (G. Qiu).

https://doi.org/10.1016/j.watres.2021.117545
Received 29 April 2021; Received in revised form 3 August 2021; Accepted 6 August 2021
Available online 12 August 2021

environments has been found through energy dispersive X-ray fluorescence spectrometry (Tabelin and Igarashi, 2009; Tabelin et al., 2012). The interaction between As(III) and pyrite depends on the Eh and pH in the mine and the surrounding water environments (Renock and Voorhis, 2017). In anoxic environments, As(III) is adsorbed or coprecipitates on pyrite surface under neutral or alkaline conditions to form a surface precipitate similar to arsenopyrite (FeAsS), while realgar (As_4S_4) or orpiment (As_2S_3) is preferably generated from the redox reaction between As(III) and pyrite under acidic conditions (Bostick and Fendorf, 2003; Kim and Batchelor, 2009). Fe(III) at the sulfur-defect sites on pyrite suface can react with adsorbed H_2O to produce the ROS $OH^{\bullet}$ and H_2O_2 (Zhang and Yuan, 2017; Zhang et al., 2016), which affects the form of co-exsiting As(III). Our previous studies have shown that dissolved O_2 promotes the production of $OH^{\bullet}$ and H_2O_2 on the pyrite and As-containing pyrite synthesized at high temperature, which could obviously accelerate As(III) oxidation and the oxidative dissolution of these synthesized iron sulfide minerals (Qiu et al., 2017). The surface properties of pyrite also significantly affect its interaction with As(III). Surface-oxidized pyrite exhibits a higher As(III) adsorption capacity than pristine pyrite (Sun et al., 2012). Therefore, different surface properties may be responsible for the difference in the reaction process of As(III) with natural and synthetic pyrite. Pyrite often coexists with some precious metals such as gold, lead and copper, but it is generally discarded as tailings due to its low economic value (Wang et al., 2020). As and pyrite in mining wastes and wastewaters can migrate to the surrounding neutral streams and rivers due to the washing of rain and the breach of tailings dam to cause secondary pollution (Hong et al., 2020; Wang et al., 2020). However, the interaction mechanism between As(III) and pyrite in near neutral natural environments remains unclear.

As a mineral of semiconductor, pyrite can be excited to produce h_{vb}^{+}–e_{cb}^{-} pairs under ultraviolet (UV) and visible light. $OH^{\bullet}$ and $O_2^{\bullet-}$ can be generated through the reactions of h_{vb}^{+} and e_{cb}^{-} with H_2O and dissolved O_2, respectively (Kirkeminde and Ren, 2013; Zeng et al., 2019). The UV-A with a wavelength range of 315–400 nm and UV-B with a wavelength range of 280–315 nm in sunlight can pass through the atmosphere and reach Earth surface (Hong et al., 2018; Hong et al., 2020). Therefore, solar irradiation affects the interaction between As (III) and pyrite in abandoned ore deposits, waste rock dumps, tailing overburdens and mining wastewaters. Previous studies have shown that light can excite pyrite and accelerate $OH^{\bullet}$ and H_2O_2 generation, thus facilitating the oxidation of Sb(III). However, the formation pathways of ROS and the ROS that plays a major role in Sb(III) oxidation require furhter investigations (Kong et al., 2015). As(III) has similar chemical properties to Sb(III). Hence, clarification of the formation and role of ROS in the interaction between As(III) and natural pyrite under solar light irradiation may help to better understand the environmental chemical behaviors of toxic elemental As and Sb in waters around mining areas.

In this study, the interaction between As(III) and natural pyrite was investigated in a near neutral pH environment under UV light in the laboratory, and the influencing factors including dissolved O_2 and pH were also studied. In the reaction, the ROS $OH^{\bullet}$, $O_2^{\bullet-}$ and H_2O_2 were detected using scavengers to clarify their possible formation pathways and contributions to As(III) oxidation. Then, the possibility that light irradiation promotes As(III) oxidation on pyrite surface in actual environments was verified under solar irradiation.

2. Methods

2.1. Pyrite pretreatment

Natural pyrite was sampled from Shangbao Village, Shaoyang City, Hunan Province, China, ground and passed through a 200-mesh sieve and then cleaned for later experiments. In the cleaning process, the pyrite was put in a centrifuge tube with acetone (30 mL), which was then shaken at 200 r min^{-1} in a constant temperature shaker for 5 min. The above cleaning process was repeated using ethanol and water instead of acetone, respectively. Finally, pyrite powder was obtained after centrifugal separation and freeze drying.

2.2. Interaction between As(III) and pyrite under UV light

As(III) (1.0 mg L^{-1}) solution was prepared by dissolving As_2O_3 solid with NaOH, and HCl solution was used to adjust the initial pH. To examine the interaction between As(III) and natural pyrite under UV light, the quartz tube with a mixture of pyrite powder (0.05 g) and 100 mL of As(III) (1.0 mg L^{-1}) solution was put in a PL-03 photochemical reactor (Beijing Precise Technology Co., Ltd., China). A mercury lamp was used as the UV light source, with the visible light being removed by a filter. The UV wavelength ranged from 237 to 400 nm, and the irradiation intensity at 365 nm was measured to be 2.5 mW cm^{-2} with a radiometer (Hong et al., 2018). A high-pressure mercury lamp was placed in a quartz cold trap, and the temperature of circulating water in the cold trap was maintained at 20°C. Although the temperature in the solution increased with reaction, no obvious difference was observed in the temperature of the reaction systems under UV irradiation and dark conditions according to our previous study (Hong et al., 2018). During the reaction, air was constantly pumped into the quartz tube. After reaction for 0, 0.25, 0.5, 1, 2, 4, 6, 8 and 12 h, 3 mL suspension was taken from the reaction system, and filtered with a millipore filter (0.22 μm). The collected solids were freeze-dried after washing using deoxygenated water.

The above photochemical reaction was also performed in nitrogen (99.999%) and oxygen atmospheres to clarify the influence of dissolved O_2. The concentration of dissolved oxygen was determined to be 0.1 ppm with a JENCO 9010 M dissolved oxygen meter in the reaction system in nitrogen atmosphere. In order to avoid the introduction of other ions to interfere with the experimental results, no buffer was added to these reactions with different pH values, and only the initial pH was adjusted to 5.0 and 9.0. To investigate the effect of actual solar irradiation, the suspension containing the mixture of As(III) (1.0 mg L^{-1}) and pyrite (0.5 g L^{-1}) was placed under sunlight in air for 8 h. The reaction time was 09:30–17:30 on March 25, 2021 with outdoor temperature of 13–20°C. The maximum light irradiation intensity at 365 and 420 nm was 2.0 and 3.9 mW cm^{-2}, respectively.

2.3. Analysis and characterization

A Shimadzu 6100 X-ray diffractometer (XRD) was applied to characterize the crystalline phase of the solid products. Analysis of functional groups and chemical composition of solid products was performed with a Bruker VERTEX 70 Fourier transform infrared spectrometer (FTIR). The observation of sample micromorphology was conducted with a Hitachi SU8000 field emission scanning electron microscope (FESEM). The chemical composition on the sample surface was analyzed by a VG Multilab2000 X-ray photoelectron spectroscopy (XPS). Charge calibration was carried out with 284.80 eV (C 1s binding energy). The Avantage software was used to fit the XPS As $3d_{(5/2)}$, Fe $2p_{(3/2)}$, S $2p_{(3/2)}$ and O 1s spectra (Chandra and Gerson, 2011; Hong et al., 2021; Qiu et al., 2017; Wang et al., 2020; Zhang et al., 2018a), and the detailed fitting processes are presented in the Supporting Information. The UV−vis scans of reaction systems containing single As(III) (0.3 mg L^{-1}), single pyrite (0.15 g L^{-1}), and the mixture of As(III) (0.3 mg L^{-1}) and pyrite (0.15 g L^{-1}) were collected using an Agilent Cary 8454 spectrophotometer. The composition of the solid product after photochemical reaction was analyzed using X-ray absorption fine structure (XAFS) spectra collected on Beijing Synchrotron Radiation Facility (BSRF, 1W1B beamline). The measurement and analysis details for XAFS are presented in the Supporting Information.

The As content in pristine pyrite was determined after microwave digestion with hydrochloric acid, nitric acid and hydrofluoric acid (volume ratio 3:1:1) at 190°C. A Haiguang AFS-8530 atomic

fluorescence spectrometer (China) was employed to analyze the concentrations of As(III) and total As (As(T)) in solution (Hen et al., 2011). The concentration of dissolved Fe^{2+} and total Fe (Fe(T)) was measured on an UV-vis spectrophotometer (Mapada UV-1800) at the wavelength of 510 nm, with 1,10-phenanthroline as the developer. Hydroxylamine hydrochloride was applied to reduce possible Fe^{3+} to Fe^{2+} in the solution during the determination of Fe(T) (Tamura et al., 1974). More descriptions about the methods for As and Fe determination are provided in the Supporting Information. As previously reported, NaOH solution can recover > 95% of the As adsorbed on pyrite surface without any change in valence (Sun et al., 2012). Therefore, the amount of adsorbed As was determined after desorption with NaOH (0.1 mol L^{-1}) solution in nitrogen atmosphere for 1 h (Qiu et al., 2018). Superoxide dismutase (SOD) at 25 mg L^{-1}, *tert*-butanol (TBA) at 10 mmol L^{-1} and KH_2PO_4 at 1.0 mmol L^{-1} were used as the scavengers for $O_2^{\bullet-}$, $OH^{\bullet}$ and Fe^{2+}, respectively, to qualitatively analyze their roles in the oxidation of As (III) (Hong et al., 2018; Ryu and Choi, 2004; Zhang et al., 2018b). Quantitative determination of H_2O_2 was performed with a DPD (*N, N*-diethyl-p-phenylenediamine) method on an UV-vis spectrophotometer (Garg et al., 2016). After the addition of sodium benzoate (BA, 10 mmol L^{-1}), the generated *p*-hydroxybenzoic acid (PBA) was determined with a high performance liquid chromatography (Agilent 1260 infinity), and the corresponding cumulative concentration of $OH^{\bullet}$ was 5.87 folds that of PBA in the reaction system (Shu et al., 2019).

3. Results

3.1. As(III) oxidation on natural pyrite under UV light

The reactions involving As(III) and/or pyrite at initial pH 7.0 were performed under UV light in air to study the influence of UV irradiation from sunlight. Fig. 1 and Fig. S1 present the concentrations of dissolved As species. No As was detected in the solution containing single pyrite after reaction for 12 h, which was consistent with the trace As (0.7 mg g^{-1}) detected in pristine pyrite, while 0.04 mg L^{-1} As(V) was detected in the system containing single As(III). After reaction in the system with the mixture of As(III) and pyrite for 12 h, the dissolved As(III) and As(V) concentrations were 0.94 and 0.03 mg L^{-1} under dark conditions, while were 0.31 and 0.46 mg L^{-1} under UV light, respectively. NaOH was used to desorb As from the surface of the solids generated from the reaction system containing the mixture of As(III) and pyrite under UV light for 12 h. The adsorption amounts of As(III) and As(V) were 0.06 and 0.17 mg L^{-1}, respectively (Fig. S2). Therefore, the total concentration of As(V) formed under UV light reached 0.63 mg L^{-1}, indicating a significant promotion of As(III) oxidation on natural pyrite under UV light irradiation.

To evaluate the effect of co-existing As(III) on pyrite, XRD, FTIR, FESEM and XPS were employed to analyze the crystalline phase, surface micromorphologies and composition of the solid products generated in the suspension containing the mixture of As(III) and pyrite under dark conditions or UV light for 12 h. No diffraction peak for other minerals occurred in the XRD patterns, while the diffraction intensity of pyrite decreased under UV light (Fig. 2a). In the XRD patterns for pristine pyrite and the pyrite after reaction with As(III) under dark and UV light conditions, the half peak width of (2 0 0) crystal plane was 0.153°, 0.173° and 0.196°, that of (−1 −1 3) crystal plane was 0.167°, 0.181° and 0.241°, and that of (−1 0 2) crystal plane was 0.164°, 0.179° and 0.191°, respectively. The XRD results indicated a slight decrease in the crystallinity of pyrite under UV light. In the FTIR spectra (Fig. S3), the peaks at 3430 and 1631 cm^{-1} correspond to the vibration of O−H in H_2O; the band at around 1100 cm^{-1} results from the vibration of SO_4^{2-}; and the band at 810 cm^{-1} is associated with the vibration of As(V)−O−Fe (Qiu et al., 2017; Wei et al., 2019a). The increase in the vibration at 810 cm^{-1} indicated an increase in As adsorption on pyrite under UV light. Massive crystals were observed in the FESEM image of pristine pyrite (Fig. 2b). After reaction under dark conditions, there were no

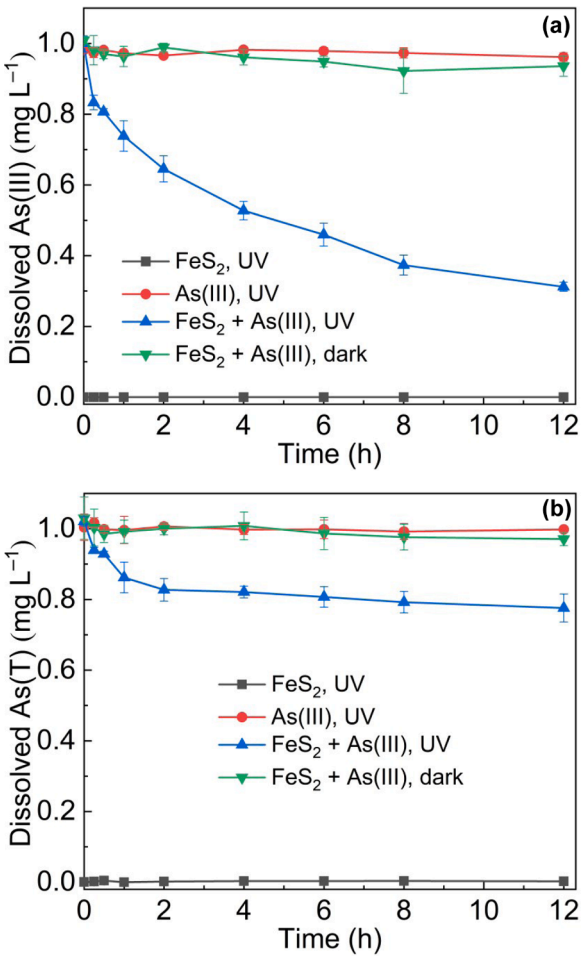

Fig. 1. Concentrations of dissolved As(III) (a) and As(T) (b) in the system containing single pyrite under UV light, single As(III) under UV light, and the mixture of As(III) and pyrite under UV light and dark conditions at initial pH 7.0 in air. The initial concentrations of pyrite and As(III) were 0.5 g L^{-1} and 1.0 mg L^{-1}, respectively.

significant changes in the micromorphology of pyrite (Fig. 2c); while the size of particles slightly decreased, with the appearance of fine crystal particles on pyrite surface under UV light (Fig. 2d). Fig. 3 and Table 1 show the XPS As $3d_{(5/2)}$, Fe $2p_{(3/2)}$, S $2p_{(3/2)}$ and O 1s spetra and the corresponding fitting results of pristine pyrite and the pyrite after reaction under dark conditions and UV light. The relative content of As(As(III)−O) was 0, 45.8% and 13.2%, and that of As(As(V)−O) was 0, 54.2% and 86.8% in pristine pyrite and the pyrite after reaction under dark conditions and UV light, respectively, indicating the promotion of As(III) oxidation under UV irradiation. After UV irradiation, the relative content of Fe(Fe(II)−S) and Fe(Fe(III)−O) slightly decreased and increased, respectively, and that of S species showed slight changes compared with that under dark conditions. In XPS O 1s spectra, the increase in the relative content of O(O^{2-}) and O(OH) can be ascribed to the adsorption of As and the possible formation of iron (hydro)oxides on pyrite (Liu et al., 2021).

Cumulative $OH^{\bullet}$ and instant H_2O_2 were determined in the reaction system containing the mixture of As(III) and pyrite to study the influence of ROS on the oxidation of As(III) under UV light (Fig. 4). Under dark conditions, the maximum cumulative $OH^{\bullet}$ and instant H_2O_2 were 0.64 and 1.42 μmol L^{-1}, which were increased to 13.00 and 1.79 μmol L^{-1}, respectively, under UV light.

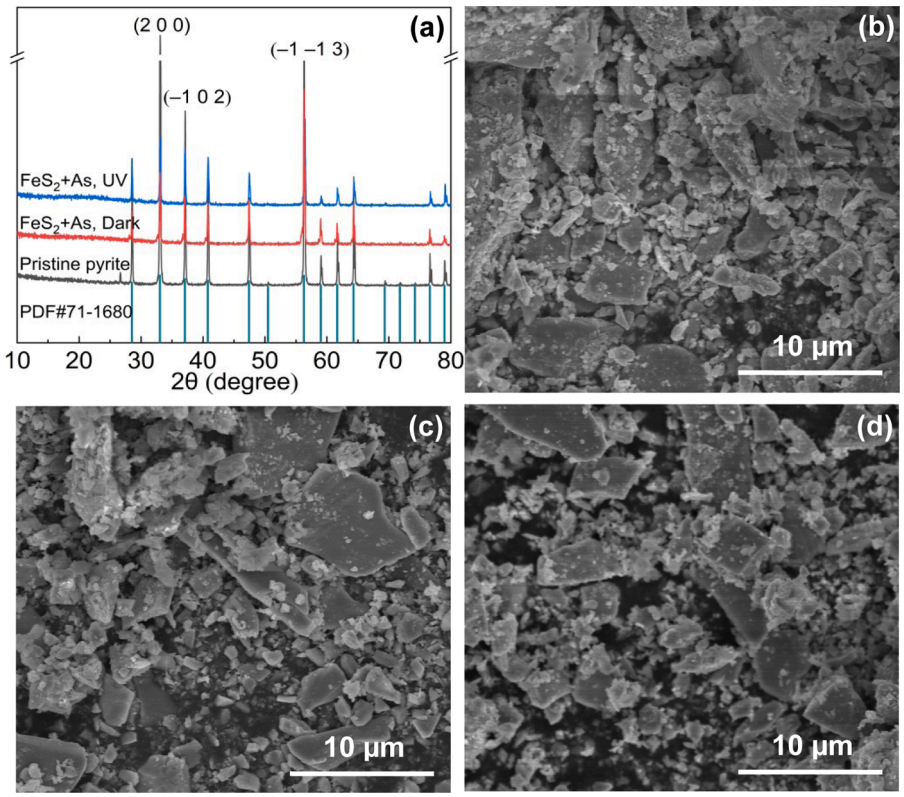

Fig. 2. XRD patterns (a) and FESEM images of natural pyrite (b) and the solid products derived from the system of As(III) (1.0 mg L^{-1}) and pyrite (0.5 g L^{-1}) under dark (c) and UV light (d) conditions at initial pH 7.0 in air.

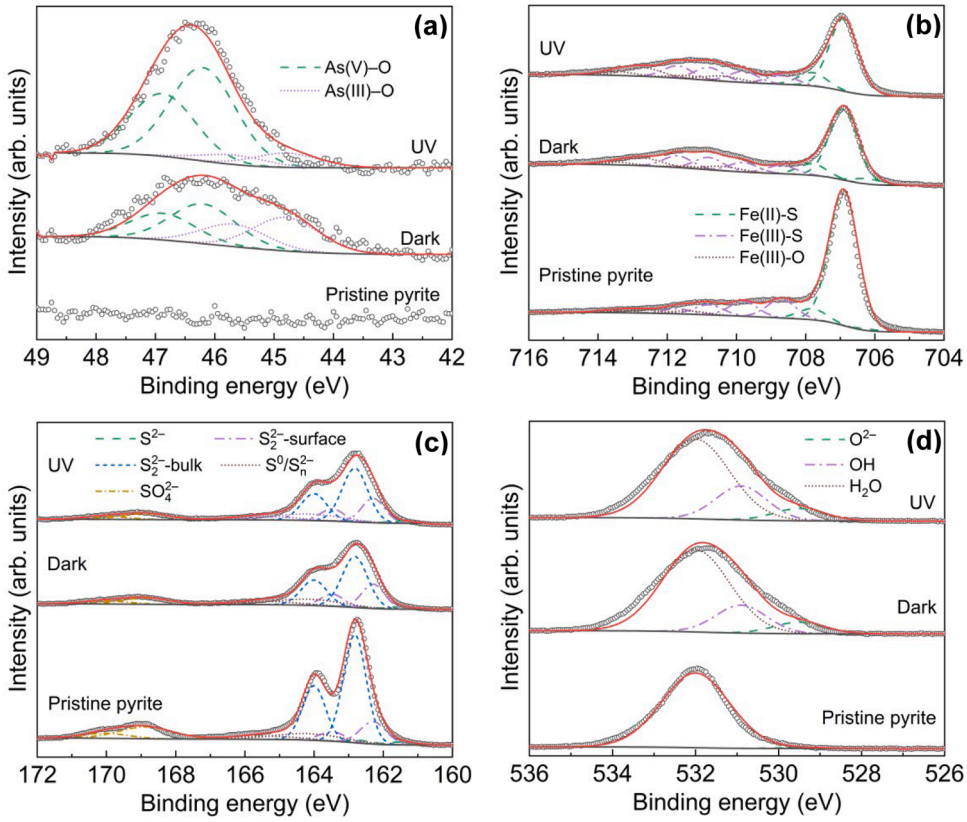

Fig. 3. XPS As $3d_{(5/2)}$ (a), Fe $2p_{(3/2)}$ (b), S $2p_{(3/2)}$ (c) and O 1s (d) spectra of natural pyrite and the solid products derived from the system of As(III) (1.0 mg L^{-1}) and pyrite (0.5 g L^{-1}) under dark and UV light conditions at initial pH 7.0 in air.

Table 1
Relative contents of As, Fe, S and O species derived from the fitting of XPS As $3d_{(5/2)}$, Fe $2p_{(3/2)}$, S $2p_{(3/2)}$ and O 1s spectra of pristine pyrite and the solid products formed in the system of As(III) (1.0 mg L^{-1}) and pyrite (0.5 g L^{-1}) under dark and UV light conditions at initial pH 7.0 in air for 12 h.

Species	Binding energy (eV)	Full width at half maximum (FWHM)	Relative content (at.%) Initial	Dark	UV
As(As(III)–O)	44.80	1.30	0	45.8	13.2
	45.68	1.30			
As(As(V)–O)	46.20	1.30	0	54.2	86.8
	46.88	1.30			
Fe(Fe(II)–S)	706.20	1.00	71.0	56.9	54.0
	706.90	1.00			
	707.80	1.00			
Fe(Fe(III)–S)	708.70	1.00	23.3	28.2	28.7
	709.80	1.00			
	710.80	1.00			
	711.70	1.00			
Fe(Fe(III)–O)	710.40	1.30	5.7	14.9	17.3
	711.40	1.30			
	712.70	1.30			
	713.50	1.30			
$S(S^{2-})$	161.49	1.00	1.6	2.4	2.0
	162.67	1.00			
$S(S_2^{2-}$-surface)	162.29	0.90	13.5	21.1	20.3
	163.47	0.90			
$S(S_2^{2-}$-bulk)	162.82	0.80	61.3	49.5	50.0
	164.00	0.80			
$S(S^0/S_n^{2-})$	164.16	2.40	11.0	16.0	15.7
	165.34	2.40			
$S(SO_4^{2-})$	168.86	1.60	12.6	11.0	12.0
	170.04	1.60			
$O(O^{2-})$	529.50	1.50	0.8	7.8	8.0
O(OH)	530.90	1.50	0	18.7	22.3
$O(H_2O)$	532.00	2.00	99.2	73.5	69.7

3.2. Effect of dissolved O_2

Nitrogen and oxygen were respectively introduced into the system containing the mixture of As(III) and pyrite to examine the effect of dissolved O_2 at initial pH 7.0 under UV light. Fig. 5a, b and Fig. S4 show the concentrations of dissolved As species. After reaction in nitrogen, air and oxygen atmospheres for 12 h, the concentrations of dissolved As(III) were 0.75, 0.31 and 0.22 mg L^{-1}, and those of dissolved As(V) were 0.07, 0.46 and 0.09 mg L^{-1}, respectively. The adsorption amount of As (III) did not show much change, while that of adsorbed As(V) increased with increasing oxygen partial pressure. After reaction in nitrogen, air and oxygen atmospheres for 12 h, the adsorption amounts of As(III) were 0.08, 0.06 and 0.06 mg L^{-1}, those of As(V) were 0.11, 0.16 and 0.20 mg L^{-1}, and the total concentrations of generated As(V) were 0.18, 0.63 and 0.70 mg L^{-1}, respectively. suggesting the acceleration of As(III) oxidation by dissolved O_2.

Fig. S5 shows the cumulative $OH^{\bullet}$ and instant H_2O_2 formed in the reaction systems with different atmospheres. In nitrogen, air and oxygen atmospheres, the maximum cumulative $OH^{\bullet}$ was 5.82, 12.98 and 18.20 μmol L^{-1}, and the maximum instant H_2O_2 was 1.09, 1.78 and 2.77 μmol L^{-1}, respectively.

3.3. Effect of pH

The initial pH of the reaction system containing the mixture of As(III) and pyrite was adjusted to 5.0 and 9.0 to investigate the influence of pH on the reaction process in air. As shown in Fig. S6, the pH decreased in the first hour, then gradually reached equilibrium in the reaction system with initial pH of 5.0, 7.0 and 9.0, and the final pH was about 4.8, 5.5 and 6.3, respectively. Fig. 5c, d and Fig. S7 show the concentrations of dissolved As species. The concentrations of dissolved As(III) and As(V) decreased with increasing initial pH. After reaction at initial pH 5.0, 7.0 and 9.0 for 12 h, the concentrations of dissolved As(III) were 0.36, 0.31 and 0.25 mg L^{-1}, and those of dissolved As(V) were 0.51, 0.46 and 0.44 mg L^{-1}, respectively. An increase in initial pH increased the amounts of adsorbed As(III) and As(V). After reaction at initial pH 5.0, 7.0 and 9.0 for 12 h, the adsorption amounts of As(III) were 0.04, 0.06 and 0.08 mg L^{-1}, those of As(V) were 0.09, 0.17 and 0.22 mg L^{-1}, and the total concentrations of generated As(V) were 0.60, 0.63 and 0.67 mg L^{-1}, respectively. These results indicated that the oxidation of As(III) and adsorption of As(III,V) on pyrite rose with increasing initial pH under UV light.

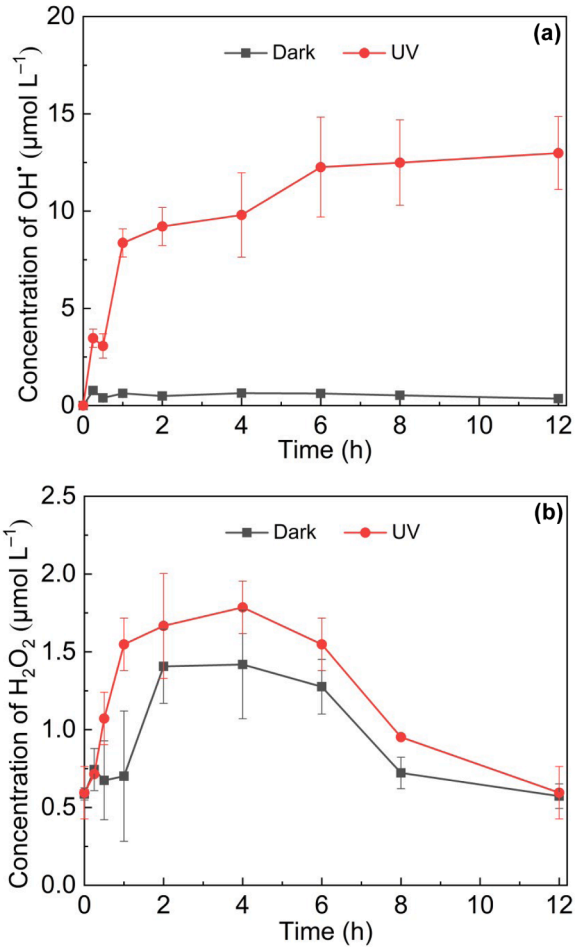

Fig. 4. Cumulative concentration of $OH^{\bullet}$ (a) and instant concentration of H_2O_2 (b) in the system of As(III) (1.0 mg L^{-1}) and pyrite (0.5 g L^{-1}) under dark and UV light conditions at initial pH 7.0 in air.

Fig. S8 shows the cumulative $OH^{\bullet}$ and instant H_2O_2 formed in the photochemical reactions with different initial pH values. An increase in initial pH tended to decrease cumulative $OH^{\bullet}$ while increase instant H_2O_2. The maximum cumulative $OH^{\bullet}$ was 29.55, 12.98 and 10.15 μmol L^{-1}, and the maximum instant H_2O_2 was 0.95, 1.78 and 3.93 μmol L^{-1} at initial pH 5.0, 7.0 and 9.0, respectively.

4. Discussion

4.1. Oxidation mechanism of As(III) on natural pyrite

Adsorption and redox can occur between As(III) and pyrite (Sun et al., 2012). Under dark conditions, dissloved As(V) accounted for about 4% of the initial As(III) in the suspension containing the mixture of As(III) and pyrite after 12 h, indicating the oxidation of As(III) on

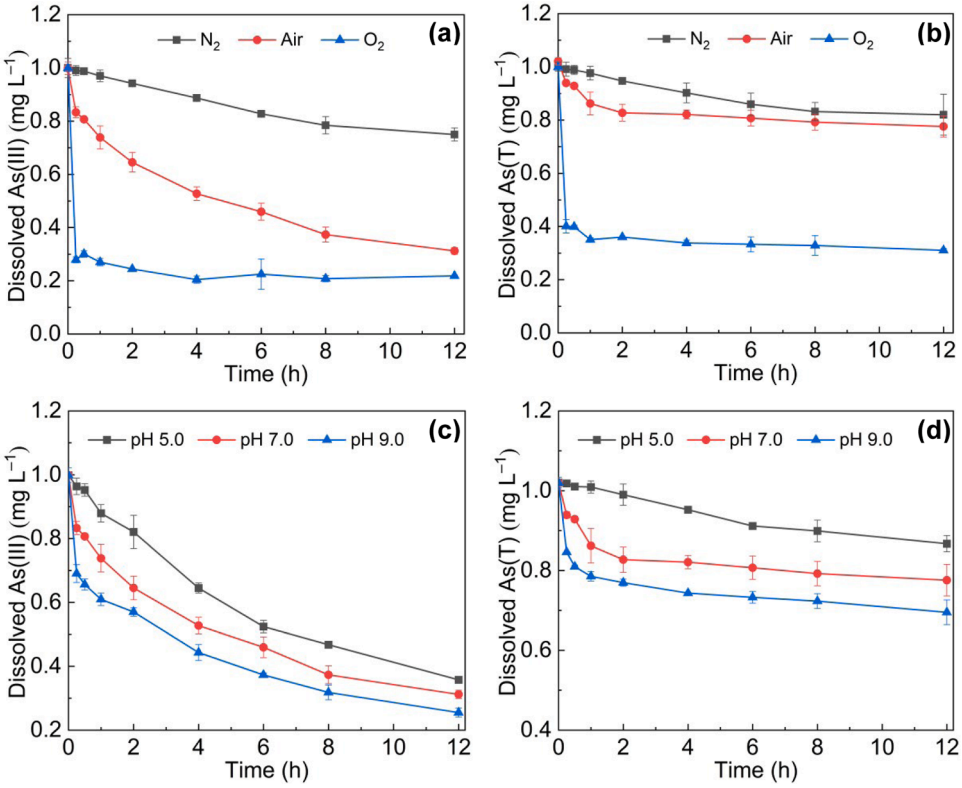

Fig. 5. Concentrations of dissolved As(III) and As(T) in the system of As(III) (1.0 mg L^{-1}) and pyrite (0.5 g L^{-1}) under UV light at initial pH 7.0 in different atmospheres (a, b) and at different initial pH values in air (c, d).

pyrite. Some previous studies have shown the presence of sulfur-defect sites on pyrite surface, where Fe(III) can react with adsorbed H_2O to form $OH^•$ (Eq. 6 in Table 2), and two $OH^•$ radicals can also combine to form H_2O_2 (Eq. 11 in Table 2) (Borda et al., 2003; Hong et al., 2018). The generation of $OH^•$ and H_2O_2 would contribute to As(III) oxidation. In our previous study, the maximum cumulative $OH^•$ and instant H_2O_2 in the reaction system containing As(III) and synthetic pyrite under dark conditions reached 60.5 and 11.3 μmol L^{-1}, respectively, which were significantly higher than those in the reaction system containing natural pyrite and As(III) (0.64 and 1.42 μmol L^{-1}, respectively) in this work (Qiu et al., 2018). As reported, the surface properties of pyrite have imporatnt impacts on its interaction with As(III). Synthesized pyrite has a higher surface activity than natural pyrite, and surface-oxidized pyrite has a higher adsorption and oxidation capacity for As(III) than pure pyrite (Kong et al., 2015; Sun et al., 2012). Therefore, the oxidation capacity of As(III) on natural pyrite in this work is lower than that on the synthesized pyrite in our previous study.

Under UV light, about 63% As(III) was oxidized, which was significantly higher than that under dark conditions. Under UV or visible irradiation, the formation process of h_{vb}^+–e_{cb}^- pairs on pyrite is similar to that on TiO_2 (Eq. 25 in Table 2). h_{vb}^+ and e_{cb}^- can react with H_2O and dissolved O_2 to produce $OH^•$ and $O_2^{•-}$, respectively (Eqs. 26 and 27 in Table 2) (Zeng et al., 2019). The oxidation of pyrite is commonly accompanied by the release of Fe^{2+} (Eqs. 1–3 in Table 2) (Kong et al., 2015; Pierre Louis et al., 2015), which will be promoted by UV light, and more $OH^•$ will be generated from the Fenton reaction (Eqs. 22 and 23 in Table 2) (Hong et al., 2018; Kong et al., 2015). In this work, Fe^{2+} could be rapidly oxidized by dissolved O_2 in near neutral environments, resulting in the production of H_2O_2 (Eqs. 19 and 20 in Table 2) (Kong et al., 2015). The ROS including $OH^•$, $O_2^{•-}$ and H_2O_2 can oxidize As(III) and some organic contaminants (Kirkeminde and Ren, 2013; Zeng et al., 2019). Compared with those under dark conditions, the concentrations of $OH^•$ and H_2O_2 increased significantly under UV light, which also indicates that UV light promotes ROS production and the subsequent oxidaiton of As(III).

KH_2PO_4 was added to the system containing the mixture of As(III) and pyrite to trap dissolved $Fe^{2+/3+}$, with the aim to investigate the main formation pathways of ROS. After the addition of KH_2PO_4, the ratio of dissolved As(III)/As(T) increased to 0.92 after 12 h, indicating a significant inhibition on As(III) oxidation. Therefore, the ROS formed under UV light might be mainly derived from the Fenton reaction or the reaction of Fe^{2+} and O_2 (Eqs. 18–23 in Table 2). TBA and SOD were respectively added into the system containing the mixture of As(III) and pyrite to further confirm the contribution of $OH^•$ and $O_2^{•-}$ to As(III) oxidation (Fig. 6). As a result, the dissolved As(III)/As(T) ratio increased from 0.31 to 0.74 and 0.65, respectively, after reaction for 12 h, indicating that $OH^•$ plays a more important role in As(III) oxidation at initial pH 7.0 in the presence of dissolved O_2.

4.2. *Effect of dissolved O_2 and pH*

In nitrogen atmosphere, the amount of oxidized As(III) on pyrite under dark conditions was lower than that under UV light, suggesting that UV light also promotes As(III) oxidation in anoxic environments. As reported, the oxidation of As(III) and Sb(III) on semiconductor minerals including goethite, magnetite and hematite can be promoted by light irradiation under anoxic conditions. In these processes, e_{cb}^- can reduce Fe(III) in iron (hydro)oxides to Fe^{2+} ($Fe(III) + e_{cb}^- \rightarrow Fe^{2+}$) under light irradiation, and h_{vb}^+ and its product $OH^•$ formed from the reaction with H_2O can oxidize As(III) and Sb(III) (Bhandari et al., 2011; Kim et al., 2010; Kong et al., 2016). Our previous study has shown that the photochemical reduction of ferrihydrite occurs under anoxic conditions, and the released Fe^{2+} can promote the transformation of ferrihydrite to lepidocrocite and goethite (Shu et al., 2019). In this work, XPS spectra proved the presence of Fe(III) on the surface of natural pyrite, and more dissolved Fe^{2+} was generated under UV light than under dark conditions in nitrogen atmosphere (Fig. S9). Therefore, pyrite promote As(III) oxidation probably through photochemical reduction in anoxic

Table 2
Chemical reactions and corresponding rate constants in As(III) and pyrite suspension.

Eq.	Reactions	K (M^{-1} s^{-1})	Ref.
	Pyrite oxidation		
1	$2FeS_2 + 7O_2 + 2H_2O \rightarrow 2Fe^{2+} + 4SO_4^{2-} + 4H^+$		(Pierre Louis et al., 2015)
2	$FeS_2 + 14Fe^{3+} + 8H_2O \rightarrow 15Fe^{2+} + 2SO_4^{2-} + 16H^+$		(Pierre Louis et al., 2015)
3	$2FeS_2 + 15H_2O_2 \rightarrow 2Fe^{2+} + 4SO_4^{2-} + 2H^+ + 14H_2O$		(Kong et al., 2015)
	Reactions on pyrite sulfur-deficient defent sites		
4	$Fe(II)_{pyrite} + O_2 \rightarrow Fe(III)_{pyrite} + O_2^{\bullet-}$		(Kong et al., 2015)
5	$Fe(II)_{pyrite} + O_2^{\bullet-} + 2H^+ \rightarrow Fe(III)_{pyrite} + H_2O_2$		(Kong et al., 2015)
6	$Fe(II)_{pyrite} + H_2O \rightarrow Fe(III)_{pyrite} + OH^{\bullet}$		(Kong et al., 2015)
	As(III) reaction		
7	$As(III) + O_2^{\bullet-} + H^+ \rightarrow As(IV) + HO_2^{\bullet}$	3.6×10^6	(Hong et al., 2018)
8	$As(III) + OH^{\bullet} + \rightarrow As(IV)$	8.5×10^9	(Hong et al., 2018)
9	$As(IV) + H_2O_2 \rightarrow As(V) + HO^{\bullet} + OH^-$		(Kim et al., 2015)
10	$As(IV) + O_2 \rightarrow As(V) + O_2^{\bullet-}/HO_2^{\bullet}$	1.1×10^9	(Hong et al., 2018)
	Reactive oxygen radical reactions		
11	$OH^{\bullet} + OH^{\bullet} \rightarrow H_2O_2$	5.2×10^9	(Kong et al., 2015)
12	$HO_2^{\bullet} + HO_2^{\bullet} \rightarrow H_2O_2 + O_2$	8.3×10^5	(Kong et al., 2015)
13	$HO_2^{\bullet} + O_2^{\bullet-} + H^+ \rightarrow H_2O_2 + O_2$	9.7×10^7	(Kong et al., 2015)
14	$OH^{\bullet} + HO_2^{\bullet} \rightarrow H_2O + O_2$	6.6×10^9	(Kong et al., 2015)
15	$OH^{\bullet} + H_2O_2 \rightarrow O_2^{\bullet-}/HO_2^{\bullet} + H_2O$	3.0×10^7	(Kong et al., 2015)
16	$OH^{\bullet} + BA \rightarrow HBA + HO_2^{\bullet}$	5.9×10^9	(Shu et al., 2019)
17	$O_2^{\bullet-} + H^+ + SOD \rightarrow H_2O_2 + O_2 +$ products		(Ryu and Choi, 2004)
	Fe^{2+} oxidation		
18	$Fe^{2+} + O_2 \rightarrow Fe^{3+} + O_2^{\bullet-}$		(Kong et al., 2015)
19	$Fe^{2+} + O_2^{\bullet-} + 2H^+ \rightarrow Fe^{3+} + H_2O_2$	1.0×10^7	(Kong et al., 2015)
20	$Fe^{2+} + HO_2^{\bullet} + H^+ \rightarrow Fe^{3+} + H_2O_2$	1.2×10^6	(Kong et al., 2015)
21	$Fe^{2+} + OH^{\bullet} \rightarrow Fe^{3+} + OH^-$	3.2×10^8	(Kong et al., 2015)
	Fenton reaction		
22	$Fe^{2+} + H_2O_2 \rightarrow Fe^{3+} + OH^{\bullet} + OH^-$		(Hong et al., 2018)
23	$Fe(OH)^+ + H_2O_2 \rightarrow Fe(OH)^{2+} + OH^{\bullet} + OH^-$		(Kong et al., 2015)
	Reaction on pyrite under solar irradiation		
24	$HO_2^{\bullet} + O_2^{\bullet-} + H^+ \rightarrow H_2O_2 + O_2$		(Zeng et al., 2019)
25	$2FeS_2 + h\nu \rightarrow FeS_2(h_{vb}^+) + FeS_2(e_{cb}^-)$		(Zeng et al., 2019)
26	$H_2O + h_{vb}^+ \rightarrow OH^{\bullet} + H^+$		(Zeng et al., 2019)
27	$O_2 + e_{cb}^- \rightarrow O_2^{\bullet-}$		(Zeng et al., 2019)

environments. As(III) can oxidize pyrite in the absence of oxygen at low pH ($\leq$ 3.5) and Eh (0.1 V *vs.* reversible hydrogen electrode) under dark conditions (Bostick and Fendorf, 2003; Renock and Voorhis, 2017; Sun et al., 2012). However, the oxidation of pyrite by As(III) was not observed, and the photochemical reduction of pyrite occurred in the presence of As(III) under anoxic conditions in this work, which may be ascribed to the near neutral pH environment. Natural waters usually maintain an anoxic state due to the sedimentation of peat or eutrophication (Fendorf et al., 2010; Xu et al., 2010). Therefore, the photochemical oxidation of As(III) on pyrite may also occur in anoxic natural waters.

Dissolved O_2 also accelerated pyrite oxidation. Under dark reaction conditions, the presence of O_2 can promote the generation of $OH^{\bullet}$ and H_2O_2 on pyrite surface through the Fenton reaction and the reaction between released Fe^{2+} and dissolved O_2 (Eqs. 22 and 23 in Table 2). Under UV light, the amount of oxidized As(III) was enhanced mainly by the production of more ROS. The concentrations of $OH^{\bullet}$ and H_2O_2 increased with increasing oxygen partial pressure (Fig. S5). In addition,

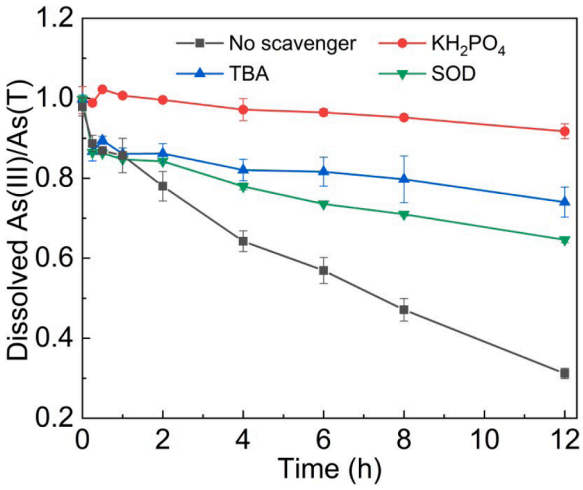

Fig. 6. Dissolved As(III)/As(T) in the system of As(III) (1.0 mg L^{-1}) and pyrite (0.5 g L^{-1}) under UV light at initial pH 7.0 in air with adding KH_2PO_4 (10 mmol L^{-1}), TBA (10 mmol L^{-1}) or SOD (25 mg L^{-1}), respectively.

O_2 can oxidize Fe(II) to Fe(III) on pyrite surface (Eq. 4 in Table 2) (Kong et al., 2015), and the surface-oxidized pyrite has higher adsorption and oxidation activity than pristine pyrite (Kong et al., 2015; Sun et al., 2012). Therefore, the improvement of As(III) oxidation on pyrite surface can be ascribed to the increase in the adsorption and oxidation activity of pyrite surface and the generation of more ROS under UV light.

As(III) oxidation was affected by pH. The photochemical oxidation of As(III) on pyrite increased slightly with increasing initial pH from 5.0 to 9.0. The dissolved Fe^{2+} released from pyrite oxidation affected the Fenton reaction and the production of $OH^{\bullet}$. The highest concentration of dissolved Fe^{2+} was 0.62 and 0.23 mg L^{-1} at initial pH 5.0 and 7.0, respectively; while no dissolved Fe^{2+} was detected at initial pH 9.0, which could be mainly ascribed to the easy oxidation of Fe^{2+} to iron (hydro)oxides at high pH values (Kong et al., 2015). Under UV light, the relative proportion of Fe(Fe(III)−O) on pyrite surface increased, confirming the generation of iron (hydro)oxides (Fig. 3). The linear combination fitting results from the XAFS spectra of the corresponding solid products further indicated that ferrihydrite was formed in the reaction system containing the mixture of pyrite and As(III) at initial pH 7.0 and 9.0 for 12 h (Fig. 7 and Table S1). $FeAsO_4$ was not detected based on the fitting results of Fe K-edge EXAFS spectra. Therefore, As was mainly adsorbed rather than co-precipitated on solid surface, and the occurrence of As(V)−O−Fe adsorption peaks in FTIR spectra can be ascribed to the adsorption of As on newly formed ferrihydrite. Besides, the negative charge of pyrite and As species increased with increasing pH, which is not conducive to the adsorption of As(III,V) on pyrite. However, the amount of adsorbed As increased significantly in this work, which was likely due to the generation of iron (hydro)oxide and its high affinity for As (Hong et al., 2020). As previously reported, the secondary minerals formed during pyrite oxidation can promote the oxidation of co-existing As(III) via galvanic interactions (Li et al., 2021; Tabelin et al., 2020; Tabelin et al., 2019). In addition, h_{vb}^+–e_{cb}^- pairs and ROS can be formed on the surface of ferrihydrite, goethite and hematite under light irradiation (Bhandari et al., 2011; 2012; Shu et al., 2019), which may also contribute to the aggravated oxidation of As(III) under light irradiation (Bhandari et al., 2011; 2012; Shu et al., 2019). With an increase in initial pH, the oxidation and precipitation of Fe^{2+} to iron (hydro) oxides on pyrite would hinder the Fenton reaction, but promote the formation of H_2O_2 through the oxidation of Fe^{2+} by dissolved O_2 (Kong et al., 2015). Therefore, the cumulative $OH^{\bullet}$ and instant H_2O_2 decreased and increased, respectively, with increasing initial pH.

To further clarify the role of ROS in As(III) oxidation at different initial pH values, TBA, SOD and KH_2PO_4 were respectively added to the

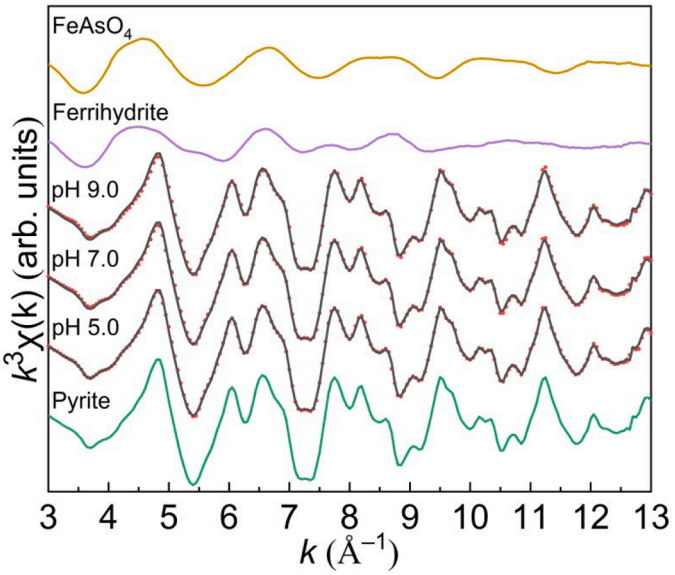

Fig. 7. Fe K-edge EXAFS spectra (red dotted lines) and the corresponding linear combination fitting (grey solid lines) of the solid products obtained from the system of As(III) (1.0 mg L^{-1}) and pyrite (0.5 g L^{-1}) under UV light at different initial pH values in air for 12 h.

reaction system containing the mixture of As(III) and pyrite with initial pH of 5.0 and 9.0 (Fig. S10). As a result, the presence of KH_2PO_4 significantly inhibited As(III) oxidation at initial pH 5.0 and 9.0. When TBA was added to the reaction system, the amount of oxidized As(III) was obviously decreased at initial pH 5.0, while only slightly decreased at initial pH 9.0. Therefore, at initial pH 5.0 and 7.0, $OH^{\bullet}$ has a major contribution to As(III) oxidation, while H_2O_2 plays a dominant role in As (III) at initial pH 9.0. The above mechanisms for ROS production and As (III) oxidation on pyrite under light irradiation are summarized in Fig. 8.

4.3. Environmental implications

Some studies have shown that sunlight affects the formation and transformation of semiconductor minerals including Fe and Mn oxides and the fate of related pollutants in natural environment (Lu et al., 2019; Shu et al., 2019; Zhang et al., 2018b). In the acid mine drainage of the Iberian Pyrite Belt (Spain), the concentration of dissolved As(III) changes periodically with the alternation of day and night, with the minimum concentration occurring at 18:00. This phenomenon is mainly due to the oxidation of As(III) to As(V) by the $OH^{\bullet}$ produced from Fe species ($Fe(III)(OH)_2 + h\nu \rightarrow Fe(II) + OH^{\bullet}$) under solar irradiation and the higher adsorption capacity of iron (hydro)oxides for As(V) than for As(III) (Sarmiento et al., 2007). Pyrite can be excited under UV and visible light (Fig. S11a), and the experimental results of pyrite and As (III) under solar irradiation showed that sunlight also promotes As(III) oxidation on pyrite (Fig. S11b). Therefore, solar irradiation can promote the oxidation of As(III) and the dissolution of pyrite in actual streams and rivers around mining areas.

In previous studies on the interaction between sulfide minerals and As, more attention has been paid to anoxic or acidic environments, providing useful information about the formation pathways of As-containing sulfide minerals and the migration and transformation process of As in acid mine drainage and groundwater (Le Pape et al., 2017; Renock and Voorhis, 2017; Sun et al., 2012). The oxidation of sulfide mineral tailings can easily lead to the release of As and the production of acid mine drainage. The As and pyrite in mining wastes and wastewaters can migrate to the near neutral waters through rain washing. In addition, the establishment of tailing dams is a common measure to treat acid mine drainage. As reported, about 200 tailing dams had breach

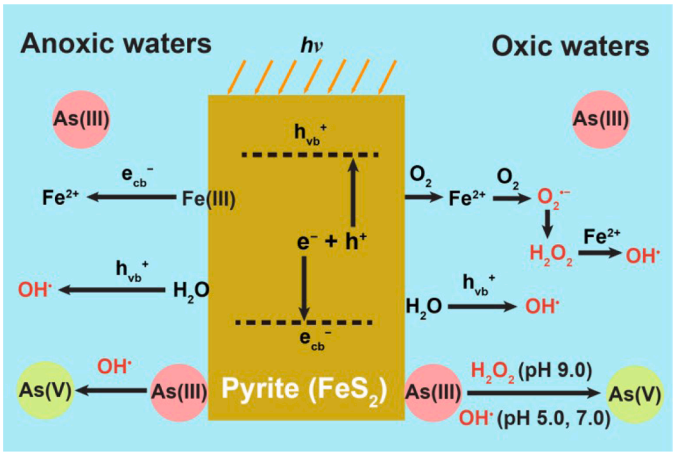

Fig. 8. Summary of mechanisms for As(III) oxidation on pyrite induced by solar irradiation.

accidents in the 20th century. The breach accidents will result in the flow of large amounts of As and sulfide minerals from mine wastewater to the near-neutral streams and rivers around the mining areas, causing secondary pollution (Azam and Li, 2010; Simmler et al., 2016). However, the adsorption and oxidation processes of As(III) on pyrite remain unclear in natural environments, particularly in those environments exposed to sunlight. This study shows that the fate of As in the near neutral streams and rivers around mining area is strongly influenced by solar irradiation. The results enrich the understanding of the further migration and transformation process of released As from the sulfide minerals in near neutral waters.

5. Conclusions

Pyrite participates in As(III) adsorption and oxidation, and solar irradiation promotes the oxidation of As(III) on pyrite. Under solar irradiation, pyrite undergoes photochemical reduction accompanied by the release of more Fe^{2+} in anoxic environments, while is photochemically oxidized in the presence of O_2. h_{vb}^+–e_{cb}^- pairs produced from the excited pyrite, Fenton reaction and the oxidation of Fe^{2+} by dissolved O_2 together lead to increases in the production of ROS including $OH^{\bullet}$, H_2O_2 and $O_2^{\bullet-}$, which contribute much to As(III) oxidation. The adsorption and oxidation activity of natural pyrite are weaker than those of synthetic pyrite, resulting in its lower oxidation capacity for As(III) relative to synthetic pyrite. The increase in oxygen partial pressure promotes ROS generation and As(III) oxidation. As(III) adsorption and oxidation on pyrite can be accelerated by increasing pH. The oxidation of Fe^{2+} to iron (hydro)oxides on pyrite leads to a decrease and increase in cumulative $OH^{\bullet}$ and instant H_2O_2, respectively, with increasing initial pH from 5.0 to 9.0. At initial pH 5.0 and 7.0, $OH^{\bullet}$ has a greater contribution to As(III) oxidation, while at initial pH 9.0, H_2O_2 plays a major role in As (III) oxidation. The iron (hydro)oxides formed on pyrite contribute to the adsorption and fixation of As(III,V) at initial pH 7.0 and 9.0. The present work provides new insights into the geochemical cycle of As(III) in mining areas.

Declaration of Competing Interest

The authors declare that they have no known competing financial interests or personal relationships that could have appeared to influence the work reported in this paper.

Acknowledgments

Financial support from the National Natural Science Foundation of China (Grant Nos. 41877025, 42077133 and 42007127), the National

Key Research and Development Program of China (Grant No. 2020YFC1808503), Leading Talent of "Ten Thousand Plan"-National High-Level Talents Special Support Plan and West Light Foundation and the Frontier Science Research Programme of the Chinese Academy of Sciences (QYZDB-SSW-DQC046) are gratefully acknowledged. The authors also thank Lihong Qin and Jianbo Cao at Public Laboratory of Electron Microscope of Huazhong Agricultural University for SEM analyses. Dr. Lirong Zheng and Dr. Shengqi Chu at BSRF (China) are acknowledged for assistance with XAFS data collection.

Supplementary materials

Supplementary material associated with this article can be found, in the online version, at doi:10.1016/j.watres.2021.117545.

References

Azam, S., Li, Q., 2010. Tailings dam failures: a review of the last one hundred years. Geotech. News 28 (4), 50–54.
Bhandari, N., Reeder, R.J., Strongin, D.R., 2011. Photoinduced oxidation of arsenite to arsenate on ferrihydrite. Environ. Sci. Technol. 45 (7), 2783–2789.
Bhandari, N., Reeder, R.J., Strongin, D.R., 2012. Photoinduced oxidation of arsenite to arsenate in the presence of goethite. Environ. Sci. Technol. 46 (15), 8044–8051.
Borda, M.J., Elsetinow, A.R., Strongin, D.R., Schoonen, M.A., 2003. A mechanism for the production of hydroxyl radical at surface defect sites on pyrite. Geochim. Cosmochim. Acta 67 (5), 935–939.
Bostick, B.C., Fendorf, S., 2003. Arsenite sorption on troilite (FeS) and pyrite (FeS_2). Geochim. Cosmochim. Acta 67 (5), 909–921.
Hellriegel, U., Figoli, A., Bundschuh, J., Hoinkis, J., 2021. Small-scale membrane-based arsenic removal for decentralized applications-Developing a conceptual approach for future utilization. Water Res. 196, 116978.
Chandra, A.P., Gerson, A.R., 2011. Pyrite (FeS_2) oxidation: a sub-micron synchrotron investigation of the initial steps. Geochim. Cosmochim. Acta 75 (20), 6239–6254.
Cuong, D.V., Wu, P.C., Chen, L.I., Hou, C.H., 2021. Active MnO_2/biochar composite for efficient As(III) removal: Insight into the mechanisms of redox transformation and adsorption. Water Res. 188, 116495.
Diao, Z., Shi, T., Wang, S., Huang, X., Zhang, T., Tang, Y., Zhang, X., Qiu, R., 2013. Silane-based coatings on the pyrite for remediation of acid mine drainage. Water Res. 47 (13), 4391–4402.
Fendorf, S., Michael, H.A., van Geen, A., 2010. Spatial and temporal variations of groundwater arsenic in South and Southeast Asia. Science 328 (5982), 1123–1127.
Garg, S., Rong, H., Miller, C.J., Waite, T.D., 2016. Oxidative dissolution of silver nanoparticles by chlorine: implications to silver nanoparticle fate and toxicity. Environ. Sci. Technol. 50 (7), 3890–3896.
Hen, C., Peng, H., Huang, W.Y., Wang, Y.J., Wu, F., 2011. Speciation of inorganic As(V)/As(III) in water and soil by hydride generation-atomic fluorescence spectrometry. Fresen. Environ. Bull. 20 (4A), 1069–1074.
Hiller, E., Lalinská, B., Chovan, M., Jurkovič, Ľ., Klimko, T., Jankulár, M., Hovorič, R., Šottník, P., Fľaková, R., Ženišová, Z., Ondrejková, I., 2012. Arsenic and antimony contamination of waters, stream sediments and soils in the vicinity of abandoned antimony mines in the Western Carpathians. Slovakia. Appl. Geochem. 27 (3), 598–614.
Ho, G.D., Tabelin, C.B., Tangviroon, P., Tamamura, S., Igarashi, T., 2021. Effects of cement addition on arsenic leaching from soils excavated from projects employing shield-tunneling method. Geoderma 385, 114896.
Hong, J., Liu, L., Luo, Y., Tan, W., Qiu, G., Liu, F., 2018. Photochemical oxidation and dissolution of arsenopyrite in acidic solutions. Geochim. Cosmochim. Acta 239, 173–185.
Hong, J., Liu, L., Ning, Z., Liu, C., Qiu, G., 2021. Synergistic oxidation of dissolved As(III) and arsenopyrite in the presence of oxygen: Formation and function of reactive oxygen species. Water Res. 202, 117416.
Hong, J., Liu, L., Tan, W., Qiu, G., 2020. Arsenic release from arsenopyrite oxidative dissolution in the presence of citrate under UV irradiation. Sci. Total Environ. 726, 138429.
Huyen, D.T., Tabelin, C.B., Thuan, H.M., Dang, D.H., Truong, P.T., Vongphuthone, B., Kobayashi, M., Igarashi, T., 2019. The solid-phase partitioning of arsenic in unconsolidated sediments of the Mekong Delta, Vietnam and its modes of release under various conditions. Chemosphere 233, 512–523.
Kim, D.H., Bokare, A.D., Koo, M., Choi, W., 2015. Heterogeneous catalytic oxidation of As(III) on nonferrous metal oxides in the presence of H_2O_2. Environ. Sci. Technol. 49 (6), 3506–3513.
Kim, E.J., Batchelor, B., 2009. Macroscopic and X-ray photoelectron spectroscopic investigation of interactions of arsenic with synthesized pyrite. Environ. Sci. Technol. 43 (8), 2899–2904.
Kim, K., Choi, W., Hoffmann, M.R., Yoon, H.-I., Park, B.-K., 2010. Photoreductive dissolution of iron oxides trapped in ice and its environmental implications. Environ. Sci. Technol. 44 (11), 4142–4148.
Kirkeminde, A., Ren, S., 2013. Thermodynamic control of iron pyrite nanocrystal synthesis with high photoactivity and stability. J. Mater. Chem. A 1 (1), 49–54.
Kong, L., He, M., Hu, X., 2016. Rapid photooxidation of Sb(III) in the presence of different Fe(III) species. Geochim. Cosmochim. Acta 180, 214–226.
Kong, L., Hu, X., He, M., 2015. Mechanisms of Sb(III) oxidation by pyrite-induced hydroxyl radicals and hydrogen peroxide. Environ. Sci. Technol. 49 (6), 3499–3505.
Le Pape, P., Blanchard, M., Brest, J., Boulliard, J.C., Ikogou, M., Stetten, L., Wang, S., Landrot, G., Morin, G, 2017. Arsenic incorporation in pyrite at ambient temperature at both tetrahedral S^{-I} and octahedral Fe^{II} sites: Evidence from EXAFS-DFT analysis. Environ. Sci. Technol. 51 (1), 150–158.
Li, X., Park, I., Tabelin, C.B., Naruwa, K., Goda, T., Harada, C., Jeon, S., Ito, M., Hiroyoshi, N., 2021. Enhanced pyrite passivation by carrier-microencapsulation using Fe-catechol and Ti-catechol complexes. J. Hazard. Mater. 416, 126089.
Liu, L., Qiao, Q., Tan, W., Sun, X., Liu, C., Dang, Z., Qiu, G., 2021. Arsenic detoxification by iron-manganese nodules under electrochemically controlled redox: mechanism and application. J. Hazard. Mater. 403, 123912.
Lu, A., Li, Y., Ding, H., Xu, X., Li, Y., Ren, G., Liang, J., Liu, Y., Hong, H., Chen, N., Chu, S., Liu, F., Li, Y., Wang, H., Ding, C., Wang, C., Lai, Y., Liu, J., Dick, J., Liu, K., Hochella Jr., M.F., 2019. Photoelectric conversion on Earth's surface via widespread Fe- and Mn-mineral coatings. Proc. Natl. Acad. Sci. U. S. A. 116 (20), 9741–9746.
Oremland, R.S., Stolz, J.F., 2003. The ecology of arsenic. Science 300 (5621), 939–944.
Paikaray, S., 2014. Arsenic geochemistry of acid mine drainage. Mine Water Environ. 34 (2), 181–196.
Park, I., Tabelin, C.B., Jeon, S., Li, X., Seno, K., Ito, M., Hiroyoshi, N., 2019. A review of recent strategies for acid mine drainage prevention and mine tailings recycling. Chemosphere 219, 588–606.
Yu, H., Shumlas, S.L., Van Aken, B., Schoonen, M.A., Strongin, D.R., 2015. Effect of phospholipid on pyrite oxidation and microbial communities under simulated acid mine drainage (AMD) conditions. Environ. Sci. Technol. 49 (13), 7701–7708.
Qiu, G., Gao, T., Hong, J., Luo, Y., Liu, L., Tan, W., Liu, F., 2018. Mechanisms of interaction between arsenian pyrite and aqueous arsenite under anoxic and oxic conditions. Geochim. Cosmochim. Acta 228, 205–219.
Qiu, G., Gao, T., Hong, J., Tan, W., Liu, F., Zheng, L., 2017. Mechanisms of arsenic-containing pyrite oxidation by aqueous arsenate under anoxic conditions. Geochim. Cosmochim. Acta 217, 306–319.
Renock, D., Voorhis, J., 2017. Electrochemical investigation of arsenic redox processes on pyrite. Environ. Sci. Technol. 51 (7), 3733–3741.
Rodriguez-Lado, L., Sun, G., Berg, M., Zhang, Q., Xue, H., Zheng, Q., Johnson, C.A., 2013. Groundwater arsenic contamination throughout China. Science 341 (6148), 866–868.
Ryu, J., Choi, W., 2004. Effects of TiO_2 surface modifications on photocatalytic oxidation of arsenite: the role of superoxides. Environ. Sci. Technol. 38 (10), 2928–2933.
Sarmiento, A.M., Oliveira, V., Gomez-Ariza, J.L., Nieto, J.M., Sanchez-Rodas, D., 2007. Diel cycles of arsenic speciation due to photooxidation in acid mine drainage from the Iberian Pyrite Belt (Sw Spain). Chemosphere 66 (4), 677–683.
Shu, Z., Liu, L., Tan, W., Suib, S.L., Qiu, G., Yang, X., Zheng, L., Liu, F., 2019. Solar irradiation induced transformation of ferrihydrite in the presence of aqueous Fe^{2+}. Environ. Sci. Technol. 53 (15), 8854–8861.
Simmler, M., Suess, E., Christl, I., Kotsev, T., Kretzschmar, R., 2016. Soil-to-plant transfer of arsenic and phosphorus along a contamination gradient in the mining-impacted Ogosta River floodplain. Sci. Total Environ. 572, 742–754.
Sun, F., Dempsey, B.A., Osseo-Asare, K.A., 2012. As(V) and As(III) reactions on pristine pyrite and on surface-oxidized pyrite. J. Colloid Interface Sci. 388 (1), 170–175.
Tabelin, C.B., Corpuz, R.D., Igarashi, T., Villacorte-Tabelin, M., Alorro, R.D., Yoo, K., Raval, S., Ito, M., Hiroyoshi, N., 2020. Acid mine drainage formation and arsenic mobility under strongly acidic conditions: Importance of soluble phases, iron oxyhydroxides/oxides and nature of oxidation layer on pyrite. J. Hazard. Mater. 399, 122844.
Tabelin, C.B., Corpuz, R.D., Igarashi, T., Villacorte-Tabelin, M., Ito, M., Hiroyoshi, N., 2019. Hematite-catalysed scorodite formation as a novel arsenic immobilisation strategy under ambient conditions. Chemosphere 233, 946–953.
Tabelin, C.B., Hashimoto, A., Igarashi, T., Yoneda, T., 2014. Leaching of boron, arsenic and selenium from sedimentary rocks: I. Effects of contact time, mixing speed and liquid-to-solid ratio. Sci. Total Environ. 472, 620–629.
Tabelin, C.B., Igarashi, T., 2009. Mechanisms of arsenic and lead release from hydrothermally altered rock. J. Hazard. Mater. 169, 980–990.
Tabelin, C.B., Igarashi, T., Tamoto, S., 2010. Factors affecting arsenic mobility from hydrothermally altered rock in impoundment-type in situ experiments. Miner. Eng. 23 (3), 238–248.
Tabelin, C.B., Igarashi, T., Tamoto, S., Takahashi, R., 2012. The roles of pyrite and calcite in the mobilization of arsenic and lead from hydrothermally altered rocks excavated in Hokkaido, Japan. J. Geochem. Explor. 119, 17–31.
Tabelin, C.B., Igarashi, T., Villacorte-Tabelin, M., Park, I., Opiso, E.M., Ito, M., Hiroyoshi, N., 2018. Arsenic, selenium, boron, lead, cadmium, copper, and zinc in naturally contaminated rocks: a review of their sources, modes of enrichment, mechanisms of release, and mitigation strategies. Sci. Total Environ. 645, 1522–1553.
Tabelin, C.B., Sasaki, R., Igarashi, T., Park, I., Tamoto, S., Arima, T., Ito, M., Hiroyoshi, N., 2017. Simultaneous leaching of arsenite, arsenate, selenite and selenate, and their migration in tunnel-excavated sedimentary rocks: I. Column experiments under intermittent and unsaturated flow. Chemosphere 186, 558–569.
Tamoto, S., Tabelin, C.B., Igarashi, T., Ito, M., Hiroyoshi, N., 2015. Short and long term release mechanisms of arsenic, selenium and boron from a tunnel-excavated sedimentary rock under in situ conditions. J. Contam. Hydrol. 175–176, 60–71.
Tamura, H., Goto, K., Yotsuyanagi, T., Nagayama, M., 1974. Spectrophotometric determination of iron(II) with 1,10-phenanthroline in the presence of large amounts of iron(III). Talanta 21 (4), 314–318.
Wang, C., Liu, R., Ahmed Khoso, S., Lu, H., Sun, W., Ni, Z., Lyu, F., 2020. Combined inhibitory effect of calcium hypochlorite and dextrin on flotation behavior of pyrite and galena sulphides. Miner. Eng. 150, 106274.

Wei, Y., Liu, H., Liu, C., Luo, S., Liu, Y., Yu, X., Ma, J., Yin, K., Feng, H., 2019a. Fast and efficient removal of As(III) from water by $CuFe_2O_4$ with peroxymonosulfate: effects of oxidation and adsorption. Water Res. 150, 182–190.

Wei, Y., Wei, S., Liu, C., Chen, T., Tang, Y., Ma, J., Yin, K., Luo, S., 2019b. Efficient removal of arsenic from groundwater using iron oxide nanoneedle array-decorated biochar fibers with high Fe utilization and fast adsorption kinetics. Water Res. 167, 115107.

Xu, H., Paerl, H.W., Qin, B., Zhu, G., Gaoa, G., 2010. Nitrogen and phosphorus inputs control phytoplankton growth in eutrophic Lake Taihu. China. Limnol. Oceanogr. 55 (1), 420–432.

Zeng, L., Gong, J., Dan, J., Li, S., Zhang, J., Pu, W., Yang, C., 2019. Novel visible light enhanced Pyrite-Fenton system toward ultrarapid oxidation of p-nitrophenol: catalytic activity, characterization and mechanism. Chemosphere 228, 232–240.

Zhang, P., Yao, W., Yuan, S., 2017. Citrate-enhanced release of arsenic during pyrite oxidation at circumneutral conditions. Water Res. 109, 245–252.

Zhang, P., Yuan, S., 2017. Production of hydroxyl radicals from abiotic oxidation of pyrite by oxygen under circumneutral conditions in the presence of low-molecular-weight organic acids. Geochim. Cosmochim. Acta 218, 153–166.

Zhang, P., Yuan, S., Liao, P., 2016. Mechanisms of hydroxyl radical production from abiotic oxidation of pyrite under acidic conditions. Geochim. Cosmochim. Acta 172, 444–457.

Zhang, W., Zhang, G., Liu, C., Li, J., Zheng, T., Ma, J., Wang, L., Jiang, J., Zhai, X., 2018a. Enhanced removal of arsenite and arsenate by a multifunctional Fe-Ti-Mn composite oxide: photooxidation, oxidation and adsorption. Water Res. 147, 264–275.

Zhang, T., Liu, L., Tan, W., Suib, S.L., Qiu, G., Liu, F., 2018b. Photochemical formation and transformation of birnessite: effects of cations on micromorphology and crystal structure. Environ. Sci. Technol. 52 (12), 6864–6871.